

# Revealing the Role of Fluoride-Rich Battery Electrode Interphases by Operando Transmission Electron Microscopy

Chen Gong, Shengda D. Pu, Xiangwen Gao, Sixie Yang, Junliang Liu, Ziyang Ning, Gregory J. Rees, Isaac Capone, Liquan Pi, Boyang Liu, Gareth O. Hartley, Jack Fawdon, Jun Luo, Mauro Pasta, Chris R. M. Grovenor, Peter G. Bruce,\* and Alex W. Robertson\*

The solid electrolyte interphase (SEI), a complex layer that forms over the surface of electrodes exposed to battery electrolyte, has a central influence on the structural evolution of the electrode during battery operation. For lithium metallic anodes, tailoring this SEI is regarded as one of the most effective avenues for ensuring consistent cycling behavior, and thus practical efficiencies. While fluoride-rich interphases in particular seem beneficial, how they alter the structural dynamics of lithium plating and stripping to promote efficiency remains only partly understood. Here, operando liquid-cell transmission electron microscopy is used to investigate the nanoscale structural evolution of lithium electrodeposition and dissolution at the electrode surface across fluoride-poor and fluoride-rich interphases. The in situ imaging of lithium cycling reveals that a fluoride-rich SEI yields a denser Li structure that is particularly amenable to uniform stripping, thus suppressing lithium detachment and isolation. By combination with quantitative composition analysis via mass spectrometry, it is identified that the fluoride-rich SEI suppresses overall lithium loss through drastically reducing the quantity of dead Li formation and preventing electrolyte decomposition. These findings highlight the importance of appropriately tailoring the SEI for facilitating consistent and uniform lithium dissolution, and its potent role in governing the plated lithium's structure.

standard hydrogen electrode), represents the ideal negative electrode for lithium-based rechargeable batteries.<sup>[1,2]</sup> However, uncontrollable dendrite formation<sup>[3,4]</sup> and continuous electrolyte depletion<sup>[5]</sup> prevents their practical realization. The solid electrolyte interphase (SEI) is the critical concept that defines these problems, as its nature fundamentally governs the chemistry that occurs at the electrode surface.<sup>[6,7]</sup> Understanding the relationship between SEI composition and the dynamic processes of Li dendrite growth and dissolution is crucial for tailoring SEIs that will allow for high cycling efficiency.


Multiple methods of SEI modification have demonstrated improved Li battery performance, such as employing a fluoride-rich electrolyte,<sup>[5,8,9]</sup> increasing the electrolyte salt concentration,<sup>[10,11]</sup> pre-constructing an artificial SEI,<sup>[12–14]</sup> and tailoring the electrolyte with additives.<sup>[15–17]</sup> Across these different approaches, it has been shown that the generation of a fluoride-rich SEI is a consistent factor for achieving improvements to Coulombic

efficiency.<sup>[18]</sup> This fluoride-rich interphase drastically reduces the formation of detached, electrically isolated “dead lithium,” and thus inhibits a major cause of efficiency loss.<sup>[19,20]</sup> Yet understanding the detailed mechanistic influence of the SEI on

## 1. Introduction

The metallic lithium anode, with its high theoretical capacity (3860 mAh g<sup>−1</sup>) and low electrochemical potential (−3.04 V vs

C. Gong, S. D. Pu, Dr. X. Gao, Dr. S. Yang, Dr. J. Liu, Z. Ning, Dr. G. J. Rees, I. Capone, L. Pi, Dr. B. Liu, G. O. Hartley, J. Fawdon, Prof. M. Pasta, Prof. C. R. M. Grovenor, Prof. P. G. Bruce, Dr. A. W. Robertson  
Department of Materials  
University of Oxford  
Parks Road, Oxford OX1 3PH, UK  
E-mail: peter.bruce@materials.ox.ac.uk; alex.robertson@materials.ox.ac.uk

 The ORCID identification number(s) for the author(s) of this article can be found under <https://doi.org/10.1002/aenm.202003118>.

© 2021 The Authors. Advanced Energy Materials published by Wiley-VCH GmbH. This is an open access article under the terms of the Creative Commons Attribution License, which permits use, distribution and reproduction in any medium, provided the original work is properly cited.

DOI: 10.1002/aenm.202003118

Dr. B. Liu, G. O. Hartley, Prof. P. G. Bruce  
Department of Chemistry  
University of Oxford  
South Parks Road, Oxford OX1 3QZ, UK

Prof. J. Luo  
Center for Electron Microscopy and Tianjin Key Lab of Advanced Functional Porous Materials  
Institute for New Energy Materials and Low-Carbon Technologies  
School of Materials Science and Engineering  
Tianjin University of Technology  
Tianjin 300384, China

Prof. P. G. Bruce  
The Henry Royce Institute  
Parks Road, Oxford OX1 3PH, UK

Prof. P. G. Bruce  
The Faraday Institution  
Quad One, Becquerel Avenue, Harwell Campus, Didcot OX11 0RA, UK

Li plating morphology and stripping uniformity remains difficult, largely due to the challenge associated with characterization of the reactive Li. Recent pioneering work has tackled this with cryogenic transmission electron microscopy (cryo-TEM),<sup>[21,22]</sup> and has revealed a marked difference in the morphology of deposited Li depending on the electrolyte used, with high-concentration electrolytes that form a fluoride-rich interphase yielding sheet-like structures rather than dendritic Li.<sup>[19]</sup> It was proposed that these less tortuous deposits are more amenable to uniform dissolution, leaving minimal dead Li, and thus ensuring good efficiency.<sup>[6]</sup>

An inherent limitation of cryo-TEM is that it is a post-mortem technique; images are acquired after the reaction, and thus are unable to capture the intermediate dynamic stages. The link between plated Li morphology and the mechanistic process by which particular Li structures are easier to strip must therefore be inferred. Given the complexity of the Li electrodeposition and stripping process, direct observation of this process would be valuable. To build a clearer understanding of the link between the morphology of deposited Li, its preference for forming dead Li on dissolution, and the overarching role of SEI composition, here we use operando liquid cell scanning transmission electron microscopy (LC-STEM) to directly image Li plating and stripping across fluoride-poor and fluoride-rich interphases. Our observations reveal that the fluoride-rich SEI promotes a denser Li deposition. These denser structures are more easily stripped than the dendritic morphologies deposited across the fluoride-poor SEI, and leave behind significantly less dead Li. Supporting our LC-STEM experiments, online mass spectrometry (MS), nuclear magnetic resonance spectroscopy (NMR), and secondary ion mass spectroscopy (SIMS), provide additional insights into the composition of the SEI and the sources of

Li loss in the two systems. These findings on the relationship between SEI composition, Li structural evolution, and the loss of Li will assist the informed design of new electrolytes and electrodes for more effective batteries.

## 2. Results and Discussion

The common Li electrolyte, LP30 (LiPF<sub>6</sub> in ethylene carbonate (EC) and dimethyl carbonate (DMC), EC:DMC = 1:1), with and without fluoroethylene carbonate (FEC) additive, was chosen as our model system.<sup>[23]</sup> FEC is understood to promote the formation of a fluoride-rich interphase with carbonate solvent Li electrolytes.<sup>[17]</sup> The real-time investigation of Li plating/stripping was carried out by cyclic voltammetry (CV) in an electrochemical LC-STEM cell, with the structural dynamics captured by high-angle annular dark-field scanning transmission electron microscopy (HAADF-STEM) imaging while varying the applied potential (**Figure 1**; Movies S1 and S2, Supporting Information). The darkest contrast regions correspond to Li metal, which has a lower density than electrolyte (Figure S1, Supporting Information).<sup>[24]</sup> All LC-STEM experiments were performed at low dose rates and under a high accelerating voltage (300 kV), minimizing beam damage by radiolysis.<sup>[25,26]</sup> The beam was blanked in between experiments, and a control experiment monitoring the effect of comparable dose was performed on the electrolyte (Figure S2, Supporting Information), showing no observable breakdown products from the beam.

For standard LP30 electrolyte, Li deposits initially nucleated at the edge of the Pt working electrode (WE) and then grew rapidly, forming micron-sized Li grains with poor intergrain connectivity (Figure 1a, panels 2–4). The growth rate of the Li grains was measured (Figure S3, Supporting Information), showing that denser root growth dominates the initial stages.

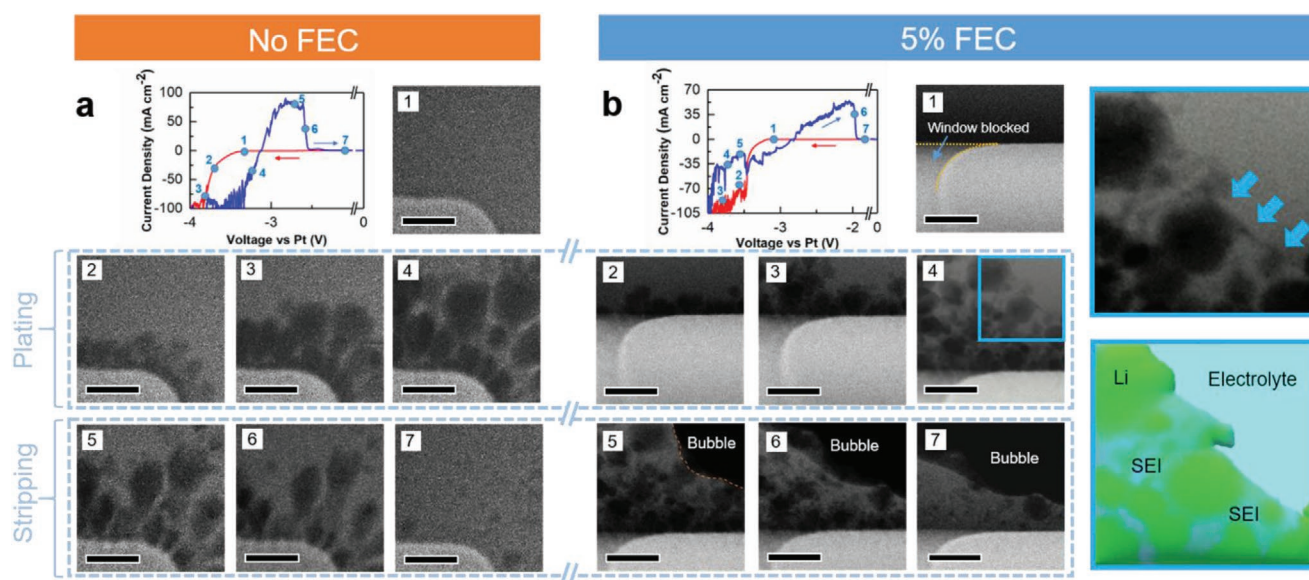


**Figure 1.** In situ liquid-cell HAADF-STEM images showing the first cycle of lithium plating/stripping in LP30 with and without 5% FEC additive. Lithium plating and stripping in a) LP30 electrolyte and b) LP30 with 5% FEC additive, with corresponding cyclic voltammogram. The magnified blue box shows the deposition morphology, with an accompanying graphic to aid interpretation (also see Figure S4, Supporting Information). Image panel numbers correspond to their respective positions on the CV plots. The Pt electrode in (b) is partly obscured by the liquid cell window edge (see Figure S5, Supporting Information). Scale bars are 2  $\mu\text{m}$ .

As the plating process continued, the focus of Li deposition moved to the tips, forming larger separated grains (Figure 1a, panel 3–4), which is likely the result of redistribution of electric field.<sup>[27]</sup> During stripping (Figure 1a, panels 5–7), the plated Li grains steadily reduced in size, dissolving from both the roots and tips. A small amount of dead Li detached from the Pt electrode and thus became electrically insulated. As we show later, these dead Li particles are no longer involved in the cell electrochemistry, leading to an overall efficiency loss.

Identical experiments were carried out to compare the effect of FEC on the first Li plating and stripping cycle (Figure 1b). The morphology of the plated Li closely resembles that shown in Figure 1a, forming coarse micron-sized grains with poor interconnectivity, and subsequent stripping similarly leaves behind dead Li deposits. The magnified insert (blue box, Figure 1b) and corresponding cartoon show the boundary interphase structure of the deposited Li, with its grains surrounded by a lower-contrast layer. The contrast signal of this micron-thick layer suggests an organic envelope surrounding the Li deposit, which could be an outer SEI.<sup>[28]</sup> Capturing any outer organic layer is challenging by conventional *ex situ* or *postmortem* techniques, as cell dismantling and sample preparation can remove it.<sup>[3,29]</sup> A marked difference between the two systems is the formation of a gas bubble in the 5% FEC experiment (Figure 1b, panels 5–7). A control experiment, where the liquid cell was subjected to an identical CV sweep but with the electron beam blanked, revealed similar bubble formation upon imaging at the end of the sweep (Figure S6, Supporting Information). Therefore bubble formation was not the result of beam-induced radiolysis gas products, but due to gas producing electrochemical side-reactions.<sup>[30–32]</sup> Side reactions are difficult to accurately diagnose in any experiment due to their complexity. However, several instances of the literature have explored this area, suggesting surface reactions of FEC on the anode can form gases such as CO<sub>2</sub> and H<sub>2</sub>.<sup>[33,34]</sup> The constrained thin volume of the liquid cell means the produced gases from across the electrode can more easily coalesce into a single bubble. The presence of a bubble may have an effect on Li plating and stripping behavior, and so to address any potential impact, we have included a detailed analysis based on the direct observation of a bubble's influence and by comparison of cycles with a bubble present (Figures S7–S9, Supporting Information, and accompanying discussion). Our analysis demonstrates that if the bubble has any effect on Li plating and stripping performance, it must be secondary to the dominant influence of the SEI.

The Li plating/stripping in the second cycle showed distinct behavior to that observed for the first cycle for both no FEC and the 5% FEC electrolytes (Figure 2; Figure S10 and Movies S3 and S4, Supporting Information). A large amount of dead Li was formed after second-cycle stripping in the no FEC case, but by contrast, little was observed with the presence of FEC (Figure S10h, Supporting Information). To better understand this difference, the lithium morphology evolution during the stripping process was investigated (Figure 2). As illustrated in Figure 2a, rather than exhibiting the granular structure seen in the first cycle, the plated Li in LP30 has a loosely packed needle-shaped morphology. During stripping, Li is not necessarily removed exclusively from the dendrite tip; other parts may be stripped first, cutting off the conductive path to the

dendrite tips and areas further away from the electrode surface. These isolated particles become dead Li, and no longer grow or shrink with cycling. This uneven stripping can be attributed to the sparse dendritic morphology, which leads to the electron channel easily being severed. By contrast, the fluorinated system shows a denser Li deposit, where the plated Li pieces are well connected with each other. This relatively flat and uniform Li deposit morphology allows most of the Li to easily maintain electric contact with the WE during stripping. As a result, the stripping proceeds smoothly from the tips to the base (as shown in Figure 2f–i; Movie S4, Supporting Information), which minimizes dead Li formation. The contrast signal of the Li deposits also constantly decreases during stripping, further indicating a uniform stripping process.

All the plating/stripping processes occur through a formed SEI, and while it is difficult to analyze this layer in detail under LC-STEM, some observations can be made, in particular regarding the thicker organic outer SEI.<sup>[28,30,35]</sup> In the FEC system, the organic SEI layer grows thicker over the course of cycling (Figure S10e–h, Supporting Information), while no SEI layer is directly seen in the additive-free study. However, we can infer its presence through observing the movement of dead Li pieces left from the previous cycles, and which were pushed away from the electrode during the following plating cycle (Figure 2k; Movies S3 and S5, Supporting Information). Their coordinated movement indicates the existence of an underlying SEI matrix that acts as a scaffold, moving the encapsulated dead Li pieces with it during cycling, as studied in prior work.<sup>[36]</sup> Analysis of the dead Li movement suggests a difference between the two electrolytes. For the no additive case, the dead Li was pushed away during plating but does not return on stripping (Figure 2k). Similarly, the dead Li is pushed away during plating in the FEC case, yet it can be seen to partially return during the stripping cycle, indicating that the SEI may be more elastic, as suggested in previous studies (Figure 2l).<sup>[15,37]</sup> This process can be seen more clearly in the real-time recording (Movie S6, Supporting Information).

To gain a deeper understanding of how FEC affects SEI composition, and how this subsequently influences the lithium plating and stripping processes, a comprehensive characterization of the SEI by NMR, online MS, SIMS, and electrochemical impedance spectroscopy (EIS) were conducted with Li||Cu coin cells using LP30 electrolyte with and without 5% FEC.

To confirm the formation of a fluoride-rich interphase after adding FEC, depth profile SIMS analysis using a plasma focused ion beam (PFIB) was used to quantitatively compare the <sup>19</sup>F/<sup>7</sup>Li<sup>−</sup> ratios from plating with the LP30 (Figure 3a) and LP30 plus 5% FEC electrolytes (Figure 3b). Both samples were Li plated for 20 min at 1 mA cm<sup>−2</sup> in Li||Cu coin cells. Quantification using SIMS is challenging as different ion species can exhibit different ionization yields, and the nature of the matrix may also effect the yield or sensitivity (the so-called matrix effect).<sup>[38]</sup> This matrix effect explains the increase in the <sup>19</sup>F/<sup>7</sup>Li<sup>−</sup> ratio we see towards the interface with the Cu foil. Using the same SIMS depth profiling conditions (working distance, working voltage, current, dwell time, etc.), we can semi-quantitatively compare the levels of fluoride enrichment in the two systems using the <sup>19</sup>F/<sup>7</sup>Li<sup>−</sup> ratios. The <sup>19</sup>F/<sup>7</sup>Li<sup>−</sup> ratio in the FEC system is significantly higher than that without FEC,



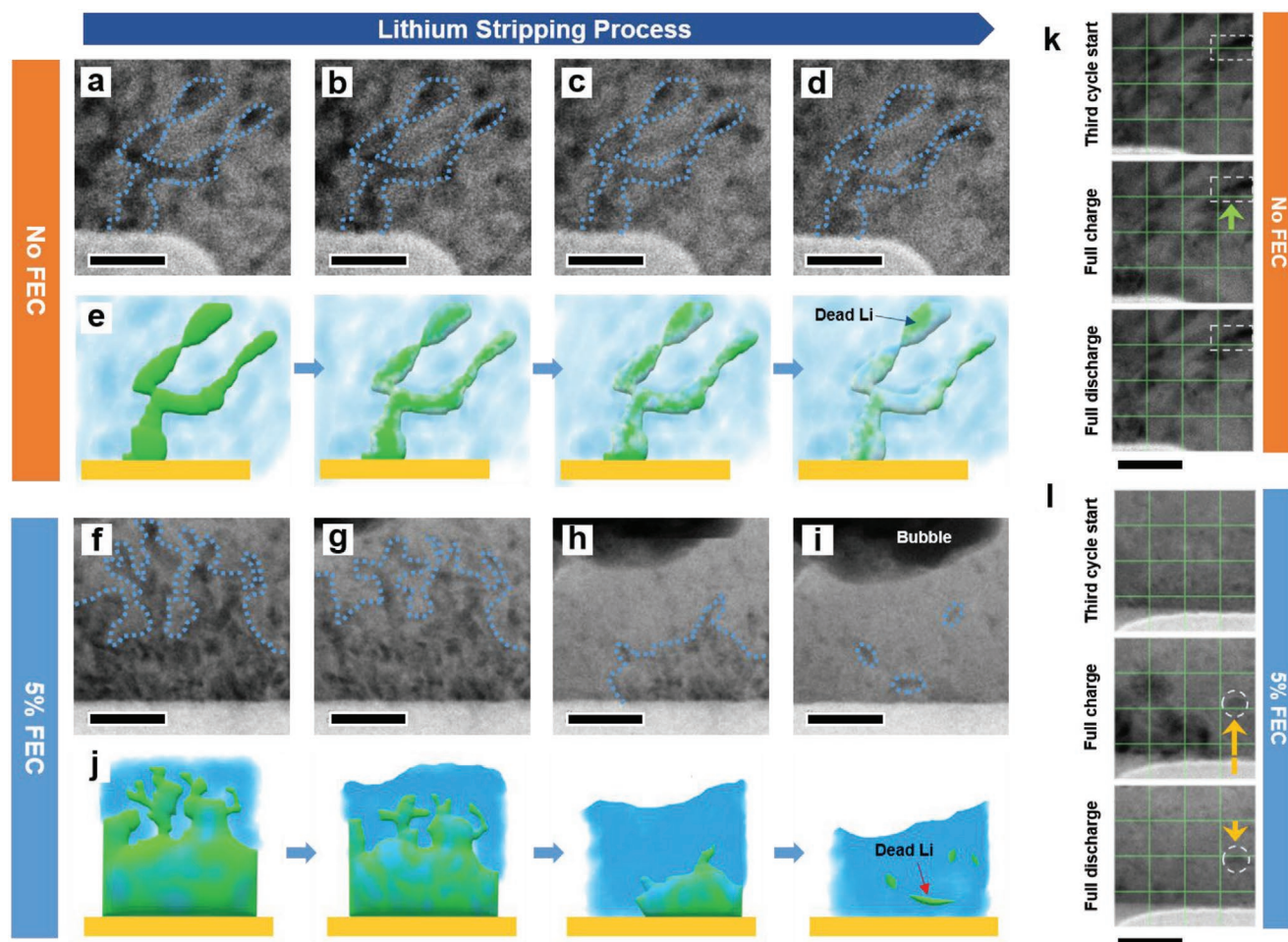


**Figure 2.** LC-STEM of the lithium structural evolution in the second and third cycles. a–j) Stripping process in the second cycle, showing the influence of FEC on lithium morphology and dead lithium generation. Dead Li movement in the third cycles in k) LP30 and l) LP30 with 5% FEC. Panels (a–d) and (f–i) are frames captured from the real-time stripping process (Movies S3 and S4, Supporting Information). Panels (e) and (j) are corresponding cartoon illustrations. Scale bar is 2  $\mu\text{m}$ .

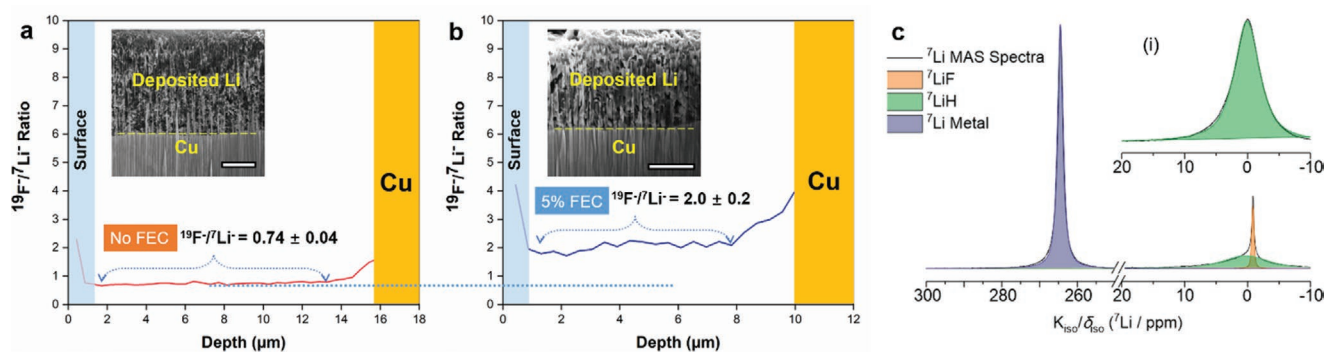


**Figure 3.** Characterization of the SEI chemical composition. a,b) PFIB-SIMS depth profiles quantifying the relative amount of fluoride ions in deposited lithium from LP30, with and without 5% FEC additive, by comparison of negative ion  $^{19}\text{F}/^{7}\text{Li}^+$  ratio. a) The  $^{19}\text{F}/^{7}\text{Li}^+$  ratio measured at  $0.74 \pm 0.04$  in the deposited Li in LP30. b) The  $^{19}\text{F}/^{7}\text{Li}^+$  ratio has a platform at  $2.0 \pm 0.2$  with the presence of FEC. Inserts show SEM images of the cross sections of deposited Li layer from which the SIMS profiling data were acquired. Scale bars are 5  $\mu\text{m}$ . c) The  $^7\text{Li}$  magic angle spinning ( $\nu_R = 10$  kHz) NMR ( $\nu_0 = 155.5$  MHz) spectrum of plated lithium. The resonance at  $K_{\text{iso}} = 264$  ppm is vertically aligned Li metal (with respect to the magnetic field,  $B_0$ ).<sup>[39]</sup> The peak at  $\delta_{\text{iso}} = -1$  ppm is in good agreement with that of  $\text{LiF}_{(s)}$ .<sup>[40]</sup> A further broader  $^7\text{Li}$  resonance is centered between 0 and 1 ppm and is in good agreement with bulk  $\text{LiH}_{(s)}$  shown in the i) inset.

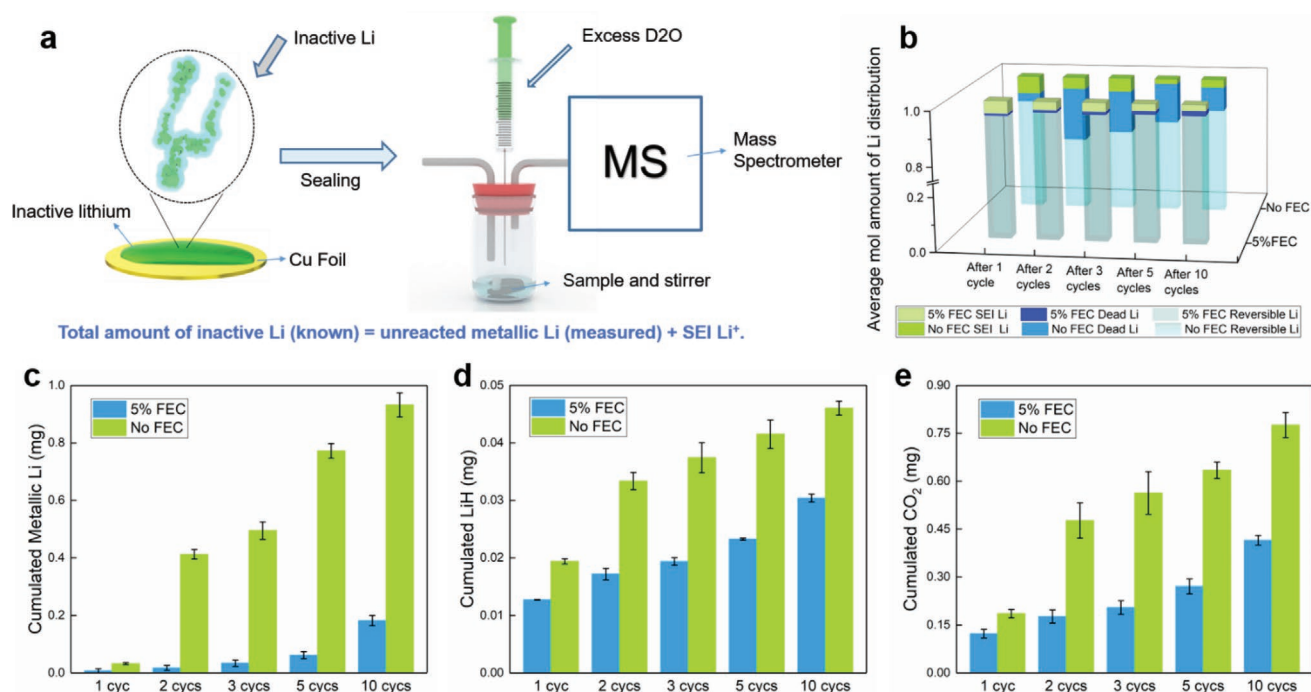


**Figure 4.** Quantification of metallic lithium and certain SEI components by online MS. a) A schematic illustrating how to quantifiably measure components on cycled Cu foil from Cu||Li cells. Li was plated and stripped at 1 mA cm<sup>-2</sup> for 2 h. b) The measured Li distribution ratio after the specified number of cycles for each electrolyte. c–e) Measured cumulative metallic Li, LiH, and organic SEI components such as (CH<sub>2</sub>OCO<sub>2</sub>Li)<sub>2</sub> and LiOCO<sub>2</sub>R following the specified number of cycles.

confirming that FEC additive yielded a fluoride-rich SEI. Solid-state magic-angle spinning NMR of <sup>7</sup>Li confirms the presence of LiF on the plated Li surface (Figure 3c). LiF is regarded as a critical component of a high-performance SEI layer, as discussed later.

Our operando STEM experiments revealed a significant difference in dead Li formation between the two electrolytes. To explore this at the coin-cell level, we performed online MS (Figure 4a) by adding deuterated water (D<sub>2</sub>O) to cycled electrode specimens and measured the resultant gas evolution. This permitted quantitative identification of the sources of Li loss—whether by detachment and electrical isolation (dead Li), or by being consumed in an expanding SEI.<sup>[41,42]</sup> Measuring the evolved gases with MS allows us to identify the various gas species, which can be assigned as products from particular reactions that correspond to the amount of unreacted metallic Li (which we assume to be exclusively dead Li), lithium hydride (LiH), and some SEI organic species such as (CH<sub>2</sub>OCO<sub>2</sub>Li)<sub>2</sub> and LiOCO<sub>2</sub>R (we will refer to as “C-organic SEI” here). Further details are presented in the methods. We compared the amount of metallic dead Li, LiH, and “C-organic SEI” from LP30 with and without 5% FEC additive after completing 1, 2, 3, 5, and 10 cycles (Figure 4c–e). A trend can be seen for all these components; for plating in LP30 with and without FEC additive, the amount of all three (metallic Li, LiH, “C-organic SEI”) increased with number of cycles. The increase in LiH and organics indicates that in both systems, the SEI growth is a continuous process. However, plating through a fluoride-rich SEI showed significantly smaller increases of these SEI components; over ten cycles, FEC effectively reduced dead Li formation

by more than 80%, LiH formation by 34% and C-organic formation by around 47%. From Figure 4b,c, we find that far less dead Li forms when a fluoride-rich SEI is present, consistent with our previous STEM results, and that this dead Li consumed a smaller proportion of the irreversible Li in the system. It is worth mentioning that these two systems both showed the presence of LiH in the SEI, as was further confirmed by NMR (Figure 3c). There have been few investigations into the possible influence of LiH in Li battery performance; however, recent cryo-STEM studies have suggested that LiH can form into dendrites and cause significant capacity loss.<sup>[3]</sup> Our results quantifiably demonstrate that less LiH is formed when FEC additive is employed, suggesting an additional benefit of a fluoride-rich interphase for promoting high cycling efficiency.

The PFIB-SIMS and online MS studies, taken together with our operando STEM observations, demonstrate that the fluoride-rich SEI formed during the first cycle significantly affects the following Li plating and stripping dynamics (Figure 5). Our real-time observations underline the importance of the structural dynamics of lithium growth during deposition and stripping, with a clear preference for a uniform and denser morphology. These stockier morphologies ensure that a path is always available for electrons to reach the Li, allowing for dissolution to take place.<sup>[19]</sup> By contrast, the dendritic structures observed in the fluoride deficient SEI were more susceptible to electrical isolation during stripping. While our TEM imaging provides direct confirmation of the beneficial role of a fluoride-rich SEI on facilitating the formation of reliably strippable Li structures, understanding how the SEI facilitates this remains complex. There is an increasing understanding around the

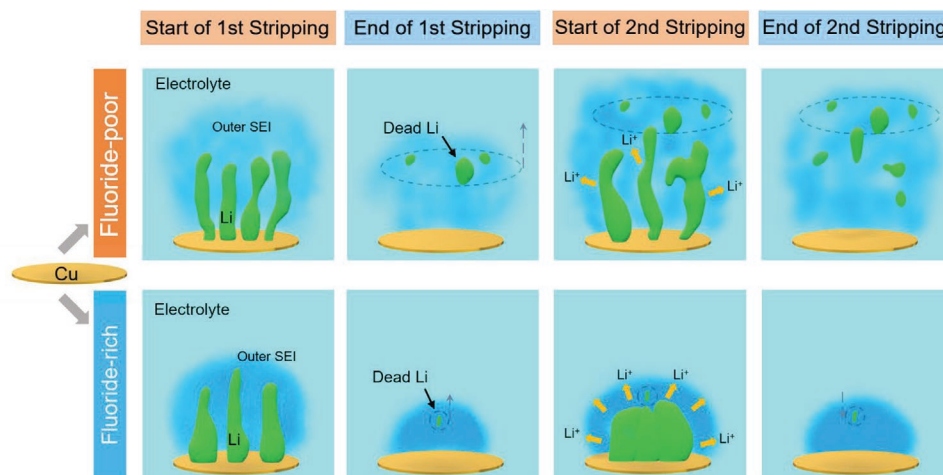


**Figure 5.** Lithium plating and stripping with different SEIs. The first electroplating and stripping cycle yields similar Li deposition morphologies while the SEI forms. From the second cycle onwards, we observe a significant difference in plating morphology, and also stripping uniformity. This results in significantly reduced dead Li formation, and can be attributed to the composition of the SEI.

likely importance of LiF as an SEI constituent,<sup>[18]</sup> and while it has a poor ionic conductivity at the bulk scale, recent work has shown that it forms nanoparticles dispersed through the SEI, meaning in practice interfacial and other mechanisms are more likely to dominate ionic conductivity.<sup>[43]</sup> Our PFIB-SIMS and NMR results suggest that our fluoride-rich SEI likely contains more LiF, and EIS measurements (Figure S11, Supporting Information) demonstrate a marked improvement in the ionic conductivity. Based on our TEM observations, the fluoride-rich SEI provides a more homogenous ionic conductivity distribution, leading to the formation of flatter structures on plating, and preventing “hot spots” of ionic conductivity during stripping that could cause Li isolation. The mechanical role of the SEI may also influence performance, with a durable and elastic layer more able to accommodate the volume change during cycling. Less continued SEI formation occurred with the fluoride-rich interphase, as the elastic SEI will ensure that reactive Li is less frequently left exposed to electrolyte, leaving fewer opportunities for excess SEI to form.

### 3. Conclusion

We have directly imaged the real-time dynamics of Li plating and stripping and how this is affected by the presence of a fluoride-rich interphase. By comparing Li cycling across fluoride-poor and fluoride-rich interphases, we have demonstrated that the fluoride-rich SEI suppresses dead Li formation and decreases electrolyte decomposition. Imaging the dynamics of Li cycling revealed that the fluoride-rich SEI yields a flatter and denser plated Li structure that presents a better morphology for uniform stripping, thus resulting in a significant reduction in dead Li. These observations are consistent with a fluoride-rich interphase being more uniform and durable, facilitating homogeneous ionic transport across the entire Li surface, and thus emphasizes the importance of understanding the SEI's composition and properties in battery design.

### 4. Experimental Section

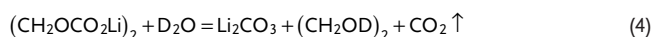
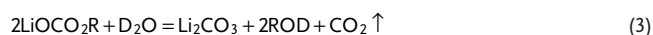
**Electrochemistry:** All the electrolyte preparation and cell assembly/disassembly was performed in an argon-filled glovebox ( $\text{H}_2\text{O} < 0.1$  ppm,  $\text{O}_2 < 0.1$  ppm). The prepared electrolytes were 1 M LiPF<sub>6</sub> in EC/DMC = 50/50 v/v (battery grade, Sigma-Aldrich) with and without 5 wt% FEC (anhydrous,  $\geq 99\%$ , Sigma-Aldrich). The water content of prepared electrolytes was measured by Karl Fischer titration (C30S Coulometric KF Titrator, Mettler Toledo) with methanol-free reagents three times each, each showing a water content value of  $< 5$  ppm. During the electrolyte preparation process, all the tools used (which include syringes, vials, tweezers, etc.) were dried in a vacuum oven for over 12 h prior to bringing into glovebox. The coin cells for online MS were Li||Cu CR2032 coin cells with two pieces of glass microfiber separators (Whatman GF/D, dried under vacuum oven). They were plated at 1 mA cm<sup>-2</sup> for 2 mAh cm<sup>-2</sup> and then stripped at 1 mA cm<sup>-2</sup> to 1 V. The coin cells for PFIB-SIMS were plated for 20 min, using Li||Cu CR2032 coin cells with a piece of separator (Celgard 3501). The CV and EIS measurements were performed on a Biologic VMP3 system.

**Real-Time Liquid-Cell STEM:** By using a Protochips Poseidon 510 holder, the electrolyte could be flown into the encapsulated liquid-cell TEM setup with a syringe pump, as our previous work shows.<sup>[44]</sup> Then, a fresh thin layer of electrolyte could be confined between two Si-SiN chips (as shown in Figure S5, Supporting Information) inside the TEM vacuum column. The flow rate used was 120  $\mu\text{L h}^{-1}$  during STEM imaging and 240  $\mu\text{L h}^{-1}$  for electrolyte refreshing after each cycle ( $\approx 15$  min flow at 240  $\mu\text{L h}^{-1}$  between each CV cycle, with beam blanked). Before we introduced electrolyte, dried DMC was flowed for 40 min at 240  $\mu\text{L h}^{-1}$  flow rate. A Gamry Reference 600 was used to provide and measure the cyclic voltammogram signal between the reference, working and counter Pt electrodes patterned on the chip. The bright field (BF) and HAADF STEM imaging was performed with a JEOL 3000F (300 kV) using a 50 micron condenser aperture. The STEM beam current was calibrated by a Faraday cup (10 pA). All of the images were recorded with a pixel dwell time of 3  $\mu\text{s}$  per pixel and at 512  $\times$  512 pixels (calculated pixel size of  $1.2 \times 10^4 \text{ \AA}^2$ ). These imaging conditions correspond to a radiation dose of  $\approx 1.6 \times 10^{-2} \text{ e}^- \text{ \AA}^{-2}$  (the beam effect is shown in Figure S2, Supporting Information). All the electrolyte preparation was performed in an argon glovebox or sealed systems. CV was performed at a scan rate of 20 mV s<sup>-1</sup>, between 0 V, -4 V, and returning to 0 V.

**Online MS:** The procedure for online MS (built in-house) is illustrated in Figure 4a. First, the cycled Li||Cu coin cell was disassembled in an argon glovebox. Then, the copper foil and the glass fiber separators on the Cu side were transferred into a well-sealed vial (along with a



magnetic stirrer) without further treatment. After the vial was connected to the MS, the gas composition inside the vial was analyzed and recorded. When the gas content was stable (checking no D<sub>2</sub>, O<sub>2</sub>, CO<sub>2</sub> and almost 100% Ar carrier gas), excess degassed D<sub>2</sub>O (>99.96 atom % D, Sigma-Aldrich) was injected into the vial and then the released D<sub>2</sub>, HD, and CO<sub>2</sub> were detected by MS (Prima BT, Thermo Fisher Scientific). Finally, the quantity of metallic Li, LiH, and some organic SEI species from the cycling can be calculated from the amount of D<sub>2</sub>, HD, and CO<sub>2</sub> gas detected by MS, according to the following reactions<sup>[19]</sup>



The carrier gas flow rate ( $r$ ) was controlled at 1 mL min<sup>-1</sup> by a digital flow meter (Bronkhorst), so the total amount  $n$  in moles of the target gas (e.g., D<sub>2</sub>, HD) can be calculated by the following equation

$$n = \int \frac{r \times P}{V_m} dt \quad (5)$$

here,  $V_m$  is the molar volume of gas (24.79 L mol<sup>-1</sup> at 25 °C) and  $P$  is the percentage of the target gas in the carrier gas stream. More setup details can be found in a previous work.<sup>[45,46]</sup>

A “blank” experiment was run to control for any potential gas emission from other components of the cell, e.g., the separator, electrodes, etc. For this, we prepared an identical coin cell but did not subject it to cycling. This was then disassembled and characterized by online MS as per the standard experiments. The results (Figure S12, Supporting Information) showed essentially no emission of HD or D<sub>2</sub> for the control cell.

**Plasma FIB SIMS:** SIMS is a sensitive analytical method able to provide information on the distribution of light elements like Li,<sup>[47,48]</sup> which are difficult to analyze by other characterization techniques. In this study, a Thermo Scientific Helios G4 Plasma FIB DualBeam (or PFIB) system combined with a Hiden Analytical EQS quadrupole SIMS detector was employed to investigate the compositional differences of SEI formed in these two systems (LP30 with and without 5% FEC electrolyte). As an analogue for the plating process, lithium samples were deposited for 20 min with and without 5% FEC in Li||Cu coin cells, and the distribution of fluoride in these samples was investigated using SIMS depth profiling. A typical mass spectrum from a sample with 5% FEC is shown in Figure S13a, Supporting Information, and identifies the signals of interest; <sup>7</sup>Li<sup>+</sup>, <sup>16</sup>O<sup>-</sup>, and <sup>19</sup>F<sup>-</sup>. Elemental depth profiling was conducted by using the quadrupole detector to detect the atomic mass unit signals from these spectra, and an area of 15 μm×15 μm (100×100 pixels) was sputtered using a focussed beam of Xe<sup>+</sup> at 30 kV and 4 nA, and a dwell time of 0.3 ms per pixel. For both samples, these scans were repeated for several cycles (each cycle includes three frames corresponding to the three signals) from the same area, giving three stacks of images showing the distributions of each element through the thickness of the plated Li layers. ImageJ was used to create elemental depth profiles. To minimize edge-related effects during SIMS analysis, only the pixels more than 2.5 μm away from the edge of the raster regions were selected for in-depth profiling. The final SIMS crater depth was also measured using PFIB sectioning, with an example of the cross-sectional view of a SIMS crater from the 5%-FEC sample is shown in Figure S13b, Supporting Information. From this depth calibration, we can estimate that each cycle of sputtering can remove a layer ≈360 nm thick, so each elemental frame was created by the removal of a layer ≈120 nm thick.

**Magnetic Resonance Spectroscopy:** All solid-state <sup>7</sup>Li magic angle spinning (MAS,  $\nu_R = 10$  kHz) NMR ( $\nu_R = 155.5$  MHz) experiments were completed at 9.45 T using a Bruker AVANCE III HD spectrometer and a 4 mm double air bearing probe. Due to the volatility of the samples, they were packed in dry HRMAS inserts inside an argon glovebox and spun

using dry-nitrogen gas. The spectra were referenced to 1 M LiCl<sub>(aq)</sub> at  $\delta_{\text{iso}} = 0$  ppm.<sup>[49]</sup> The lithium was plated for 2 h in a Cu||Li coin cells with LP30 electrolyte (1 mA cm<sup>-2</sup>).

## Supporting Information

Supporting Information is available from the Wiley Online Library or from the author.

## Acknowledgements

C.G. and S.D.P. contributed equally to this work. The authors thank the support and acknowledge the use of the facilities of the DCCEM, at the Materials Department, Oxford (EP/R010145/1). J. Luo thanks the support of the 111 project of China (D17003). J.L. and C.R.M.G. are grateful for the support from EPSRC grant (EP/P001645/1). P.G.B. is indebted to the Engineering and Physical Sciences Research Council (EPSRC), including the SUPERGEN Energy Storage Hub (EP/L019469/1), Enabling Next Generation Lithium Batteries (EP/M009521/1), Henry Royce Institute for Advanced Materials (EP/R00661X/1, EP/S019367/1, and EP/R010145/1), and the Faraday Institution All-Solid-State Batteries with Li and Na Anodes (FIRG007 and FIRG008) for financial support. A.W.R. thanks the support of the Research and Development Program of Korea Institute of Energy Research (KIER/CO-2459), and the Royal Society.

## Conflict of Interest

The authors declare no conflict of interest.

## Data Availability Statement

Supporting research data has been deposited in the Oxford Research Archive, and is available under this <https://doi.org/10.5287/bodleian:8JxpmJeVO>.

## Keywords

batteries, dendrites, in situ TEM, Li electroplating, metal anodes

Received: September 30, 2020

Revised: December 21, 2020

Published online:

- [1] M. D. Tikekar, S. Choudhury, Z. Tu, L. A. Archer, *Nat. Energy* **2016**, 1, 16114.
- [2] D. Lin, Y. Liu, Y. Cui, *Nat. Nanotechnol.* **2017**, 12, 194.
- [3] M. J. Zachman, Z. Tu, S. Choudhury, L. A. Archer, L. F. Kourkoutis, *Nature* **2018**, 560, 345.
- [4] X.-B. Cheng, R. Zhang, C.-Z. Zhao, F. Wei, J.-G. Zhang, Q. Zhang, *Adv. Sci.* **2016**, 3, 1500213.
- [5] R. Weber, M. Genovese, A. J. Louli, S. Hames, C. Martin, I. G. Hill, J. R. Dahn, *Nat. Energy* **2019**, 4, 683.
- [6] C. Fang, X. Wang, Y. S. Meng, *Trends Chem.* **2019**, 1, 152.
- [7] Y. Li, W. Huang, Y. Li, A. Pei, D. T. Boyle, Y. Cui, *Joule* **2018**, 2, 2167.
- [8] S. Jurng, Z. L. Brown, J. Kim, B. L. Lucht, *Energy Environ. Sci.* **2018**, 11, 2600.
- [9] X. Fan, L. Chen, O. Borodin, X. Ji, J. Chen, S. Hou, T. Deng, J. Zheng, C. Yang, S.-C. Liou, K. Amine, K. Xu, C. Wang, *Nat. Nanotechnol.* **2018**, 13, 715.

- [10] X. Fan, L. Chen, X. Ji, T. Deng, S. Hou, J. Chen, J. Zheng, F. Wang, J. Jiang, K. Xu, C. Wang, *Chem* **2018**, 4, 174.
- [11] H. Zheng, H. Xiang, F. Jiang, Y. Liu, Y. Sun, X. Liang, Y. Feng, Y. Yu, *Adv. Energy Mater.* **2020**, 10, 2001440.
- [12] Y. Gao, T. Rojas, K. Wang, S. Liu, D. Wang, T. Chen, H. Wang, A. T. Ngo, D. Wang, *Nat. Energy* **2020**, 5, 534.
- [13] J. Luo, C.-C. Fang, N.-L. Wu, *Adv. Energy Mater.* **2018**, 8, 1701482.
- [14] O. Sheng, J. Zheng, Z. Ju, C. Jin, Y. Wang, M. Chen, J. Nai, T. Liu, W. Zhang, Y. Liu, X. Tao, *Adv. Mater.* **2020**, 1, 2000223.
- [15] Z. L. Brown, S. Jurng, C. C. Nguyen, B. L. Lucht, *ACS Appl. Energy Mater.* **2018**, 1, 3057.
- [16] Y. Xu, H. Wu, Y. He, Q. Chen, J. G. Zhang, W. Xu, C. Wang, *Nano Lett.* **2020**, 20, 418.
- [17] X.-Q. Zhang, X.-B. Cheng, X. Chen, C. Yan, Q. Zhang, *Adv. Funct. Mater.* **2017**, 27, 1605989.
- [18] C. Wang, Y. S. Meng, K. Xu, *J. Electrochem. Soc.* **2019**, 166, A5184.
- [19] C. Fang, J. Li, M. Zhang, Y. Zhang, F. Yang, J. Z. Lee, M. H. Lee, J. Alvarado, M. A. Schroeder, Y. Yang, B. Lu, N. Williams, M. Ceja, L. Yang, M. Cai, J. Gu, K. Xu, X. Wang, Y. S. Meng, *Nature* **2019**, 572, 511.
- [20] Y.-C. Hsieh, M. Leißing, S. Nowak, B.-J. Hwang, M. Winter, G. Brunklaus, *Cell Rep. Phys. Sci.* **2020**, 1, 100139.
- [21] Y. Li, Y. Li, A. Pei, K. Yan, Y. Sun, C.-L. Wu, L.-M. Joubert, R. Chin, A. L. Koh, Y. Yu, J. Perrino, B. Butz, S. Chu, Y. Cui, *Science* **2017**, 358, 506.
- [22] X. Wang, M. Zhang, J. Alvarado, S. Wang, M. Sina, B. Lu, J. Bouwer, W. Xu, J. Xiao, J.-G. Zhang, J. Liu, Y. S. Meng, *Nano Lett.* **2017**, 17, 7606.
- [23] K. Xu, *Chem. Rev.* **2004**, 104, 4303.
- [24] B. L. Mehdi, J. Qian, E. Nasybulin, C. Park, D. A. Welch, R. Faller, H. Mehta, W. A. Henderson, W. Xu, C. M. Wang, J. E. Evans, J. Liu, J. G. Zhang, K. T. Mueller, N. D. Browning, *Nano Lett.* **2015**, 15, 2168.
- [25] R. F. Egerton, P. Li, M. Malac, *Micron* **2004**, 35, 399.
- [26] S. Pu, C. Gong, A. W. Robertson, *R. Soc. Open Sci.* **2020**, 7, 191204.
- [27] P. Zou, Y. Wang, S. W. Chiang, X. Wang, F. Kang, C. Yang, *Nat. Commun.* **2018**, 9, 464.
- [28] Y. Zhou, M. Su, X. Yu, Y. Zhang, J. G. Wang, X. Ren, R. Cao, W. Xu, D. R. Baer, Y. Du, O. Borodin, Y. Wang, X. L. Wang, K. Xu, Z. Xu, C. Wang, Z. Zhu, *Nat. Nanotechnol.* **2020**, 15, 224.
- [29] K. Xu, *Chem. Rev.* **2014**, 114, 11503.
- [30] A. L. Michan, B. S. Parimalam, M. Leskes, R. N. Kerber, T. Yoon, C. P. Grey, B. L. Lucht, *Chem. Mater.* **2016**, 28, 8149.
- [31] Y. Jin, N.-J. H. Kneusels, L. E. Marbella, E. Castillo-Martínez, P. C. M. M. Magusin, R. S. Weatherup, E. Jónsson, T. Liu, S. Paul, C. P. Grey, *J. Am. Chem. Soc.* **2018**, 140, 9854.
- [32] Y. Jin, Z. Zheng, D. Wei, X. Jiang, H. Lu, L. Sun, F. Tao, D. Guo, Y. Liu, J. Gao, Y. Cui, *Joule* **2020**, 4, 1714.
- [33] I. A. Shkrob, J. F. Wishart, D. P. Abraham, *J. Phys. Chem. C* **2015**, 119, 14954.
- [34] E. Markevich, G. Salitra, D. Aurbach, *ACS Energy Lett.* **2017**, 2, 1337.
- [35] Y. Jin, N. J. H. Kneusels, L. E. Marbella, E. Castillo-Martínez, P. C. M. M. Magusin, R. S. Weatherup, E. Jónsson, T. Liu, S. Paul, C. P. Grey, *J. Am. Chem. Soc.* **2018**, 140, 9854.
- [36] A. W. Robertson, G. Zhu, B. L. Mehdi, R. M. J. Jacobs, J. De Yoreo, N. D. Browning, *ACS Appl. Mater. Interfaces* **2018**, 10, 22801.
- [37] T. Hou, G. Yang, N. N. Rajput, J. Self, S. W. Park, J. Nanda, K. A. Persson, *Nano Energy* **2019**, 64, 103881.
- [38] K. L. Moore, E. Lombi, F. J. Zhao, C. R. M. Grovenor, *Anal. Bioanal. Chem.* **2012**, 402, 3263.
- [39] N. M. Trease, T. K. J. Köster, C. P. Grey, *Electrochem. Soc. Interface* **2011**, 20, 69.
- [40] C. Wan, S. Xu, M. Y. Hu, R. Cao, J. Qian, Z. Qin, J. Liu, K. T. Mueller, J. G. Zhang, J. Z. Hu, *ACS Appl. Mater. Interfaces* **2017**, 9, 14741.
- [41] A. Guéguen, D. Streich, M. He, M. Mendez, F. F. Chesneau, P. Novák, E. J. Berg, *J. Electrochem. Soc.* **2016**, 163, A1095.
- [42] A. Ray, T. Bristow, C. Whitmore, J. Mosely, *Mass Spectrom. Rev.* **2018**, 37, 565.
- [43] Q. Zhang, J. Pan, P. Lu, Z. Liu, M. W. Verbrugge, B. W. Sheldon, Y. T. Cheng, Y. Qi, X. Xiao, *Nano Lett.* **2016**, 16, 2011.
- [44] S. D. Pu, C. Gong, X. Gao, Z. Ning, S. Yang, J.-J. Marie, B. Liu, R. A. House, G. O. Hartley, J. Luo, P. G. Bruce, A. W. Robertson, *ACS Energy Lett.* **2020**, 5, 2283.
- [45] Z. Peng, S. A. Freunberger, Y. Chen, P. G. Bruce, *Science* **2012**, 337, 563.
- [46] M. M. Ottakam Thotiyil, S. A. Freunberger, Z. Peng, P. G. Bruce, *J. Am. Chem. Soc.* **2013**, 135, 494.
- [47] Y. H. Lin, N. Sakai, P. Da, J. Wu, H. C. Sansom, A. J. Ramadan, S. Mahesh, J. Liu, R. D. J. Oliver, J. Lim, L. Aspirtarte, K. Sharma, P. K. Madhu, A. B. Morales-Vilches, P. K. Nayak, S. Bai, F. Gao, C. R. M. Grovenor, M. B. Johnston, J. G. Labram, J. R. Durrant, J. M. Ball, B. Wenger, B. Stannowski, H. J. Snaith, *Science* **2020**, 369, 96.
- [48] K. Li, T. Aarholt, J. Liu, H. Hulme, A. Garner, M. Preuss, S. Lozano-Perez, C. Grovenor, *Appl. Surf. Sci.* **2019**, 464, 311.
- [49] R. K. Harris, E. D. Becker, S. M. Cabral de Menezes, R. Goodfellow, P. Granger, *Solid State Nucl. Magn. Reson.* **2002**, 22, 458.